

Photocatalytic water oxidation with iron oxide hydroxide (rust) nanoparticles

Timothy L. Shelton, Bronwyn L. Bensema, Nicholas K. Brune,
Christopher Wong, Max Yeh, and Frank E. Osterloh*

University of California, Davis, Department of Chemistry, One Shields Avenue, Davis,
California 95616, United States

Abstract. Hematite has attracted considerable interest as a photoanode material for water oxidation under visible illumination. Here, we explore the limits of photocatalytic water oxidation activity with iron (III) oxide hydroxide nanocrystals and NaIO₄ as a sacrificial electron acceptor ($E = 1.63$ V NHE at pH = 0.5). The sol was prepared by hydrolysis of FeCl₃ in boiling 0.002-M HCl solution and confirmed to mainly consist of β -FeO(OH) (akaganéite) particles with 5 to 15 nm diameter. From a 0.01 M aqueous NaIO₄ solution, the sol evolves between 4.5 and 35.2 $\mu\text{mol O}_2 \text{ h}^{-1}$, depending on pH, light intensity (>400 nm, 290 to 700 mW cm⁻²), β -FeO(OH), and NaIO₄ concentration. The activity increases with pH, and depends linearly on light intensity and photocatalyst amount, and it varies with sacrificial electron donor concentration. Under optimized conditions, the apparent quantum efficiency is 0.19% (at 400 nm and 460 mW cm⁻²), and the turnover number is 2.58 based on total β -FeO(OH). Overall, the efficiency of the β -FeO(OH)/NaIO₄ photocatalytic system is limited by electron hole recombination and by particle aggregation over longer irradiation times (24 h). Lastly, surface photovoltage measurements on β -FeO(OH) films on fluorine doped tin oxide substrate confirm a 2.15 eV effective band gap for the material. © 2016 Society of Photo-Optical Instrumentation Engineers (SPIE) [DOI: [10.1117/1.JPE.7.012003](https://doi.org/10.1117/1.JPE.7.012003)]

Keywords: solar energy; photocatalysis; hematite; water splitting; surface photovoltage spectroscopy.

Paper 16053SS received May 7, 2016; accepted for publication Jun. 21, 2016; published online Aug. 16, 2016.

1 Introduction

Water photoelectrolysis provides a possible avenue to sustainable fuels created by direct conversion of solar energy.^{1,2} The water oxidation reaction is a key step in this process. Many compounds catalyze the reaction, but materials that are stable, inexpensive, and responsive to visible light are scarce. Hematite (α -Fe₂O₃) does exhibit suitable optical properties and stability,^{3,4} but the performance of this material continues to be limited by electron–hole separation, slow charge transport and slow water oxidation kinetics.⁵ Since the discovery of Fe₂O₃ as a photoanode material, efforts have been directed at improving its activity^{6–18} and at understanding the mechanism of water oxidation.^{16,17,19–28} In contrast, very few studies have been directed at water oxidation with suspended iron oxide particles. Initial observations of photocatalytic hydrogen evolution from illuminated Fe₂O₃ suspensions were likely due to the presence of organic impurities in the system.^{29–31} Ohmori et al.³² used Fe³⁺ as sacrificial acceptor to evolve O₂ from illuminated Fe₂O₃ films, but the gas evolution rate was very low (<2 $\mu\text{mol h}^{-1} \text{ cm}^{-2}$). In 2011, photochemical oxygen formation from illuminated α -Fe₂O₃ suspensions in the presence of silver nitrate as a chemical bias was reported for the first time.³³ It was found that water oxidation rates scaled inversely with particle size, indicating that hole transport to the nanoparticle surface was a limiting factor. However, the best quantum efficiency was only 0.61 % (375 nm) and the turnover number (TON) of the system was limited to 1.13 because of silver

*Address all correspondence to: Frank E. Osterloh, E-mail: fosterloh@ucdavis.edu

1947-7988/2016/\$25.00 © 2016 SPIE

deposition onto the nanocrystals. This side reaction made systematic catalytic studies impossible, and prompted a search for alternative sacrificial electron acceptors. Here, we report photocatalytic water oxidation with iron (III) oxide hydroxide ($\beta\text{-FeO(OH)}$, Akaganéite) particles, a precursor to hematite and an ingredient in rust. The $\beta\text{-FeO(OH)}/\text{NaIO}_4$ system supports photocatalytic O_2 evolution from water under visible light. The activity is linearly dependent on solution pH and illumination intensity, and monotonically increases with $\beta\text{-FeO(OH)}$ concentration. The O_2 evolution rate also increases with NaIO_4 but is limited by aggregation of the colloid at high concentration. Under optimized conditions, O_2 can be produced at a maximum rate of $35.2 \mu\text{mol h}^{-1}$ and with a quantum efficiency of 0.19% (at 400 nm), and a turnover number of 2.58 based on Fe(O)OH . This is 2 to 3 orders of magnitude below the performance of the best Fe_2O_3 photoanodes. Long-term irradiation experiments (24 h) show an activity decay that can be attributed to particle aggregation. Overall, these results confirm that photocatalytic O_2 production is possible with suspended iron (III) oxide hydroxide particles, a precursor to hematite, and that the activity is limited by electron hole recombination and particle aggregation.³⁴

2 Results and Discussion

$\beta\text{-FeO(OH)}$ nanoparticles were synthesized by hydrolysis of FeCl_3 in aqueous HCl solution, similar to the protocol by Philipse et al.³⁵ The reaction yields a colloid consisting of particles in the 5 to 15 nm range, based on transmission electron microscopy (TEM) and dynamic light scattering results in Figs. 1(a) and 1(b). Some larger particles (50 to 300 nm) are seen in the TEM but not in the dynamic light scattering experiment. According to x-ray diffraction (XRD) [Fig. 1(c)], the particles are made of hydrated iron oxide ($\beta\text{-FeO(OH)}$, akaganéite) with some hematite also present. The optical absorption spectrum [Fig. 2(a)] of the colloid shows an absorption edge at 575 nm (2.16 eV) very similar to a hematite sol.³³ Selective photoexcitation of the material without optical interference from metaperiodate or its reduction products (IO_3^- or I^-) can be achieved with the use of a 400 nm long pass filter (2M NaNO_2). Indeed, while the $\beta\text{-FeO(OH)}/\text{NaIO}_4$ mixture evolves over $10 \mu\text{mol/h}$ of O_2 under these conditions [Fig. 2(b)], only trace amounts of O_2 were observed in the absence of light, or when only $\beta\text{-FeO(OH)}$ or NaIO_4 were present. This suggests that O_2 evolution involves the light-driven redox reactions and IO_4^- as the sacrificial electron acceptor ($E = +1.19 \text{ V}$ at pH 7).

To determine the limiting factors for the photocatalytic process in more detail, oxygen evolution rates were measured as a function of light intensity. In Fig. 3(a), it can be seen that activity increases linearly with light power, as expected for a photon driven process. From the intercept of the linear fit with the x -axis, the minimum light power density for O_2 evolution is 93.63 mW cm^{-2} . However, as deviations from linearity at low illumination power are possible, quantum efficiency measurements (see following material) provide a better measure of the limiting photoactivity of the sol.

Figure 3(b) shows the dependence of the photocatalytic rate on sacrificial donor concentration. The O_2 evolution rate increases strongly with NaIO_4 concentration, until it reaches a maximum ($23.7 \mu\text{mol h}^{-1}$) at 0.04 M, and then it declines, as the IO_4^- concentration is raised above 0.05 M. This activity decrease is likely connected to the higher ionic strength of the electrolyte and a resulting stability decrease of the colloid that leads to particle aggregation [Fig. 3(c)].^{36,37} Theoretically, higher O_2 evolution rates might be achievable with a sacrificial electron acceptor that does not cause particle aggregation.

Next, in order to determine the effect of the $\beta\text{-FeO(OH)}$ concentration on O_2 evolution, sols with different particle content were illuminated at constant flux, sacrificial agent concentration, and solution pH. From Fig. 4(a), it can be seen that in the 0.035 to 0.32 mg mL^{-1} interval, the O_2 production rate increases with increasing concentration of nanoparticles, indicating that light absorption is limiting under these conditions.

Next, the pH dependence of the photocatalytic process was investigated. As seen in Fig. 4(b), the O_2 production rate is found to linearly increase with the pH of the solution. From the slope of the plot, the rate varies $1.15 \mu\text{mol h}^{-1}$ per unit pH and is highest at pH = 12.24. This trend cannot be explained by the thermodynamics of the reaction, as the pH-dependence of water oxidation and iodate reduction cancel out [Eqs. (1)–(3)]:

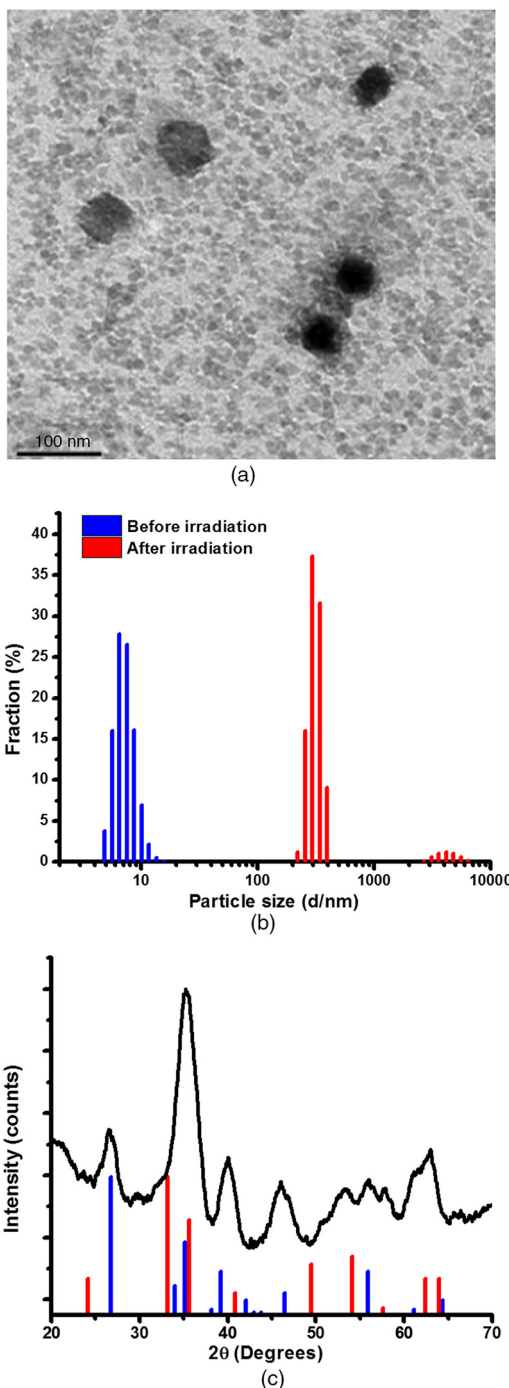
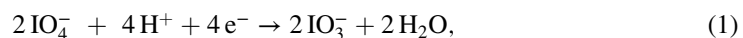


Fig. 1 (a) TEM image of β -FeO(OH) nanoparticles, scale bar is 100 nm. (b) Dynamic light scattering data (blue) show particles in the 5.6 to 8.7 nm diameter range 24 h after synthesis. After irradiation (red), particle size increases to 300–400 nm. There also appears a small portion (<5% of total particles) of much larger agglomerated particles in the 2.5 to 6.5 μ m range. (C) PXRD of β -FeO(OH) particles (black). Standard diffraction pattern for β -FeO(OH) (blue) from PDF card 00-034-1266. The pattern for α -Fe₂O₃ (red, pdf card 00-033-0664) is also shown.



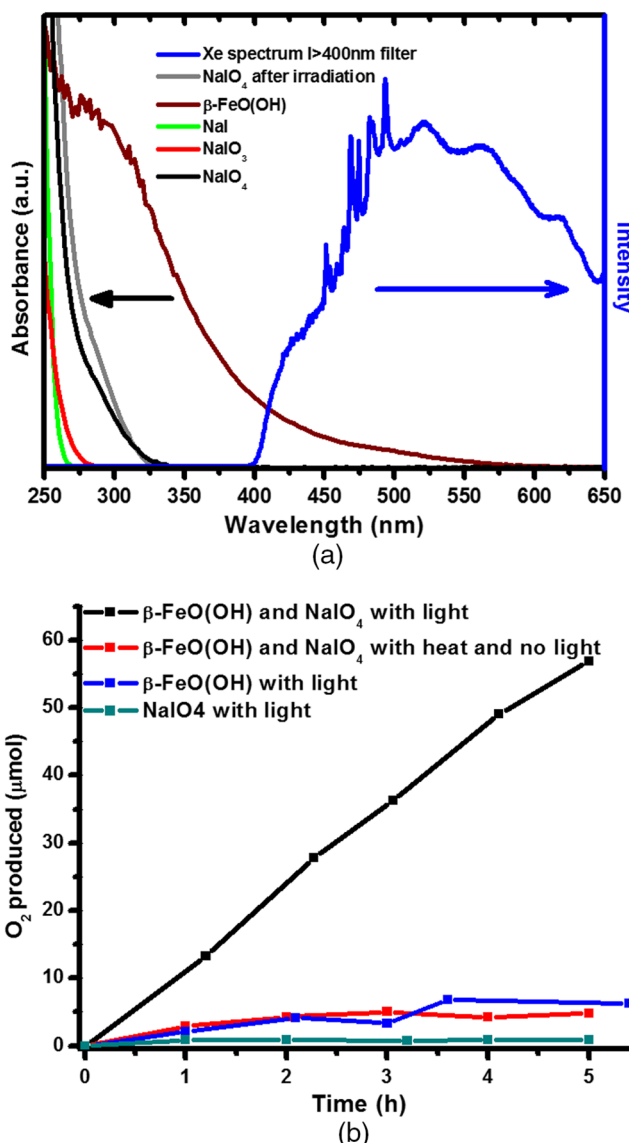


Fig. 2 (a) Optical absorbance data for $\beta\text{-FeO(OH)}$ suspension (brown trace), metaperiodate (black), iodate (red), iodide (green), and metaperiodate after 12 h irradiation (gray). The xenon lamp emission overlaps with $\beta\text{-FeO(OH)}$ in the visible region ($\lambda > 400$ nm). (b) Oxygen evolution from particle suspensions under visible (> 400 nm) illumination or in the dark, and from metaperiodate solution in an oil bath at 60°C.

Indeed, both water oxidation and IO_4^- reduction potentials exhibit near-ideal Nernstian behavior, despite changing levels of hydration with pH (at pH 0.5, iodate exists as H_3IO_4 with a reduction potential $E^0 = +1.63$ V, at pH 6 the metaperiodate IO_4^- with $E^0 = +1.30$ V is the dominant form, and at pH 13, the hydrated $\text{H}_3\text{IO}_6^{3-}$ ion with $E^0 = +0.69$ V prevails).^{38,39} Similarly, the particle band edge potentials are expected to move along with the pH.⁴⁰ Instead, the experimental pH dependence of O_2 evolution must be attributed to the “kinetics” of the water oxidation. Two types of water oxidation mechanisms, an “acidic” and an “alkaline mechanism,” which involves free or bound hydroxyl species can be distinguished.^{26,41} At pH values below seven, the hydroxide concentration becomes small and water serves as main proton acceptor for Eq. (2). Because water is less basic than hydroxide, the water oxidation rate in acidic medium is smaller than in basic solution and the activation energy for water oxidation is larger. At high pH, the more basic hydroxide becomes the preferred proton acceptor, speeding up the reaction. This explains the observed pH dependence of O_2 evolution.

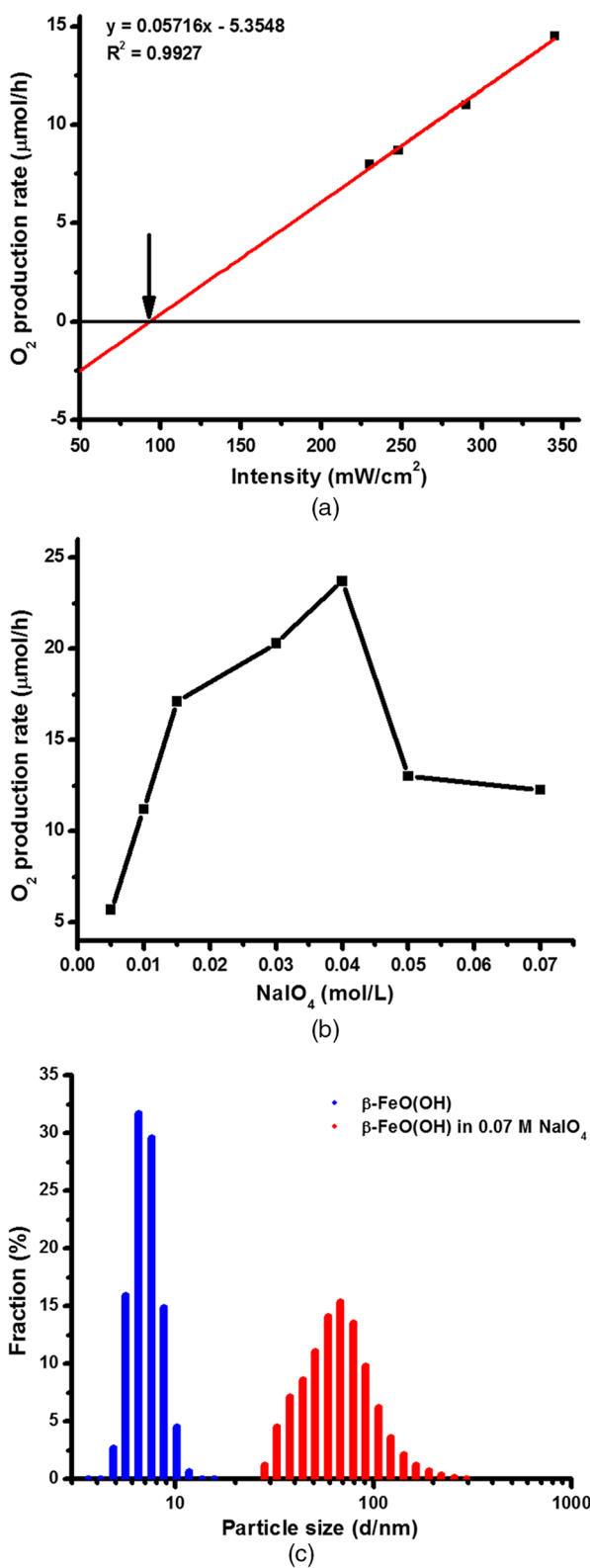


Fig. 3 Oxygen evolution from $\beta\text{-FeO(OH)}$ suspensions. (a) O_2 production rates versus irradiance intensity. Minimum photon flux estimated to be 93 mW cm^{-2} . (b) Effect of sacrificial agent concentration on O_2 production rate. (c) Particle size distribution obtained by DLS measurement of $\beta\text{-FeO(OH)}$ suspension in water (blue) and in a solution of 0.07 M NaIO_4 . Both solutions were pH adjusted to 7.9 by dropwise addition of 2 M NaOH .

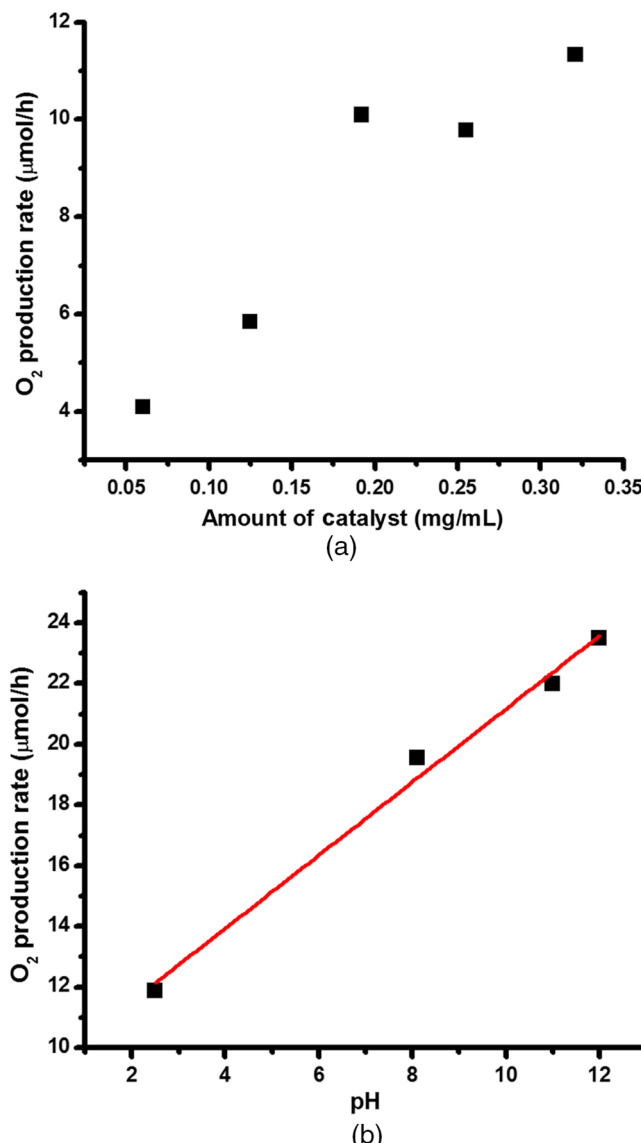


Fig. 4 Oxygen production rate with (a) variable catalyst concentration (0.01 M NaIO₄, pH 11.4, flux: 290 mW cm⁻²) and (b) pH (0.3 g L⁻¹ catalyst, 0.01 M NaIO₄ flux: 980 mW cm⁻²).

Next, we compare the O₂ evolution rate of the β -FeO(OH) sol with that of state of the art Fe₂O₃ photoanodes. Under optimized conditions, the β -FeO(OH)/NaIO₄ system evolves 35.2 $\mu\text{mol O}_2 \text{ h}^{-1}$ (Fig. 5). This corresponds to an oxygen evolution current density of 64.35 $\mu\text{A cm}^{-2}$ under \sim 7 suns illumination (680 mW cm⁻²). In comparison, state of the art Fe₂O₃ photoanodes^{17,34,42-44} have been shown to support anodic current densities of up to 5.7 mA cm⁻² at +1.23 V_{RHE} applied bias and AM 1.5 illumination. This is 2 to 3 orders of magnitude higher than the calculated photocurrent of the sol. The lower activity of the colloid can be attributed to several factors, including the lower activity of the β -FeO(OH) phase, the lack of a water oxidation cocatalyst and the lack of a fast electron extraction pathway. This causes the majority of electron hole pairs to recombine in the β -FeO(OH) nanoparticles.

In order to obtain a second estimate of the fraction of reactive e/h pairs in the sol, the quantum efficiency of oxygen evolution is measured under illumination from a 400 nm LED (460 mW cm⁻²). Under these conditions, the β -FeO(OH)/NaIO₄ system generates 5.55 $\mu\text{mol O}_2 \text{ h}^{-1}$ which corresponds to an apparent quantum efficiency of 0.19%, i.e., over 99% of the holes recombine with electrons prior to reaction with water. This QE value compares well to our previous value for the Fe₂O₃/AgNO₃ system (QE = 0.61% at 375 nm).³³ In that

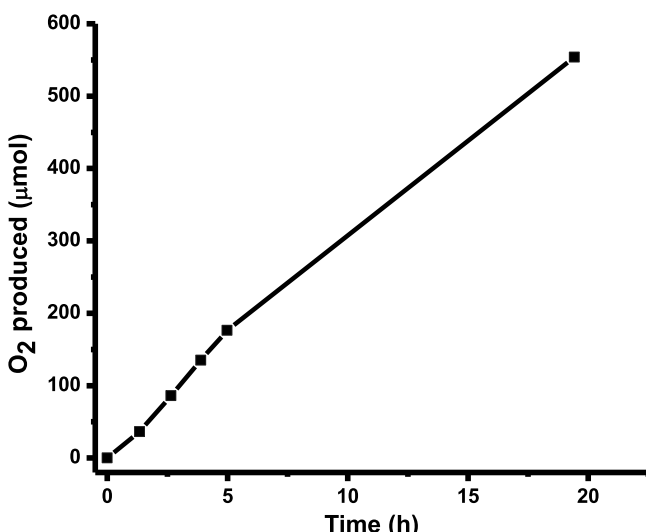


Fig. 5 Oxygen evolution from an optimized $\beta\text{-FeO(OH)}$ /NaIO₄ system. pH: 12.9, intensity: 680 mW cm⁻², NaIO₄: 0.03 M, 18.75 mg $\beta\text{-FeO(OH)}$ in 75 mL nanopure water. After 24 h, the resulting total O₂ is 553 μmol , corresponding to a TON of 2.58.

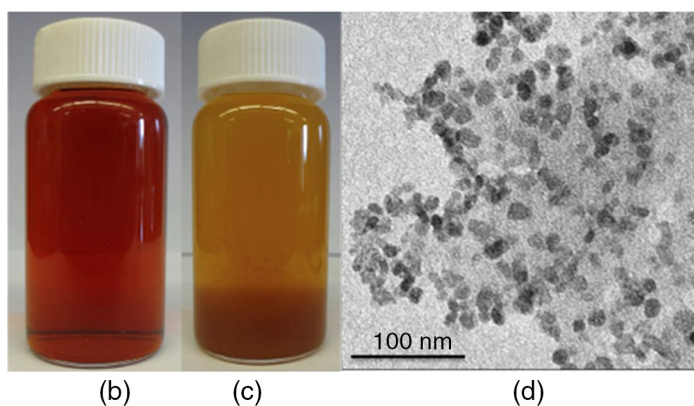
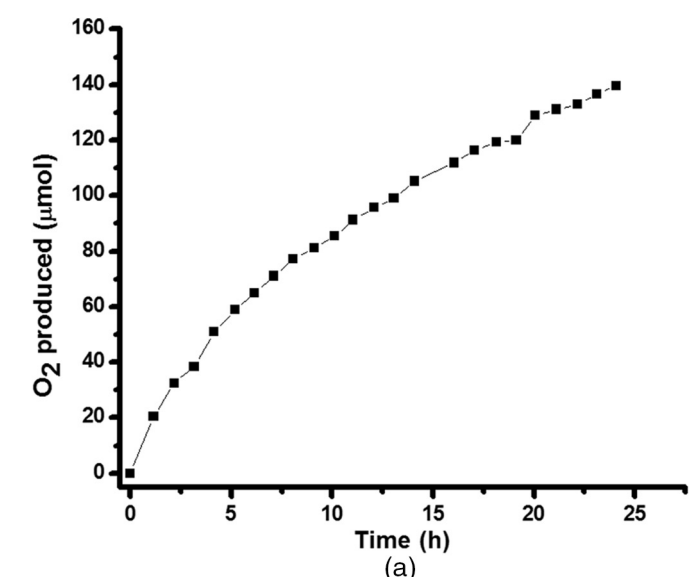


Fig. 6 (a) 24 h continuous irradiation of $\beta\text{-FeO(OH)}$ suspension. Lamp intensity: 470 mW cm⁻², pH: 12.2, NaIO₄: 0.01 M, mass of catalyst: 23.44 mg. Pictures of $\beta\text{-FeO(OH)}$ suspension (b) before and (c) after irradiation. TEM image (d) of particle aggregate.

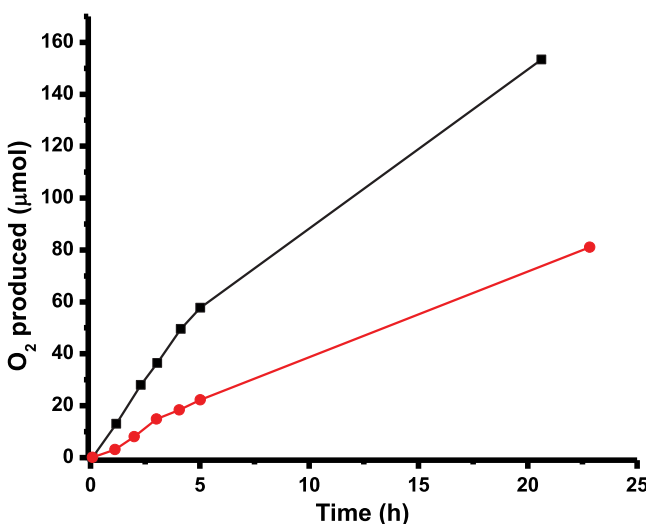


Fig. 7 Decreased oxygen evolution upon repeated irradiations of same $\beta\text{-FeO(OH)}$ sample due to aggregation of particles. 30 mg catalyst, 0.015 M NaIO₄, 600 mW cm⁻², pH 12.1

case, the QE is higher because of the better activity of the $\alpha\text{-Fe}_2\text{O}_3$ phase and due to the higher photon energy. Nevertheless, the QE values remain more than two orders of magnitude below the incident photon to current efficiency values of optimized Fe₂O₃ photoanodes (up to 80% at 400 nm).¹⁷

Next, we discuss the long-term stability of the photocatalytic water oxidation system. As can be seen from Fig. 6(a), the O₂ evolution rate slowly decays over a 24 h period from initially 11.1 to 4.33 $\mu\text{mol h}^{-1}$, a 60% decrease. This decay is accompanied by a change of the optical appearance of the suspension and is caused by agglomeration of particles into large aggregates as confirmed by TEM [Fig. 6(d)]. The aggregates are 300 to 400 nm in diameter, based on dynamic light scattering measurements after irradiation [Fig. 1(b)]. A very small portion (<5%) of aggregates in the 2.5 to 6.5 μm range is also present. While we presently do not understand the reason for the particle aggregation during irradiation, it is the likely cause for the loss of catalytic activity. Indeed, repeat irradiations of partially aggregated samples confirm a loss in activity (Fig. 7). As the particles aggregate, the specific surface area of the sol decreases, and with it the ability to effectively absorb light or transfer short-lived charge carriers into the solution. We have previously described the effect of Fe₂O₃ particle size on photocatalytic O₂ evolution.³³

Lastly, we present surface photovoltage (SPV) measurements on $\beta\text{-FeO(OH)}$ nanocrystal films deposited by drop-coating on a modified fluorine doped tin oxide (FTO) substrate.

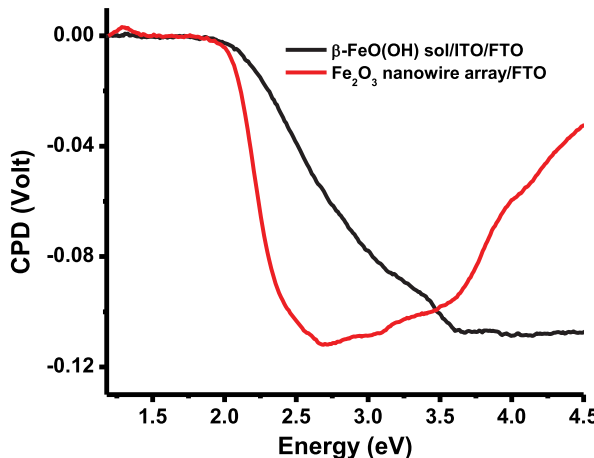


Fig. 8 SPV spectrum of $\beta\text{-FeO(OH)}$ nanoparticle film (black) on FTO/ITO substrate. The spectrum of a hematite nanowire film on FTO is shown in comparison.⁵⁰

The SPV scan in Fig. 8 shows a negative voltage signal with an onset of 2.15 eV, which reaches its most negative value of -106 mV at a photon energy of 3.75 eV. The photoonset of photovoltage has been shown to be a good predictor of the effective bandgap of semiconductors.^{45–49} The 2.15 eV value agrees well with the optical absorption onset at 575 nm [2.16 eV, Fig. 2(a)]. For comparison, Fig. 8 also shows the photovoltage spectrum on Fe_2O_3 nanowire arrays (red trace).⁵⁰ Here, the maximum photovoltage is reached at 2.7 eV instead of 3.75 eV. This suggests that photochemical charge separation in the $\alpha\text{-Fe}_2\text{O}_3$ nanowires is more efficient than in the $\beta\text{-FeO(OH)}$ particle film.

2.1 Conclusions

In summary, these experiments establish visible light-driven photocatalytic water oxidation with suspended iron (III) oxide hydroxide nanoparticles, a precursor to hematite and ingredient in rust. Oxygen evolution is favored at high pH, which is a result of the faster water oxidation kinetics. As expected, the performance of the system increases with light intensity and particle concentration. Under optimized conditions, the apparent quantum efficiency of the system is 0.19% at 400 nm and the turnover number is 2.58 after 24 h. Overall, this performance is comparable to suspended $\alpha\text{-Fe}_2\text{O}_3$ particles, but about 2 to 3 orders of magnitude lower than that of state of the art hematite photoelectrodes. According to the SPV data, the lower O_2 evolution rate is a result of a lower photovoltage of the $\beta\text{-FeO(OH)}$ phase in comparison to $\alpha\text{-Fe}_2\text{O}_3$. The lack of a water oxidation cocatalyst and inefficient electron hole separation in the small particles are additional factors. Also, the activity of the system decays over time as irradiated particles form large aggregates with lower surface area. In theory, improved $\beta\text{-FeO(OH)}$ photocatalysts could be achievable with other redox couples, such as H_2O_2 or $\text{Fe}(\text{CN})_6^{3-/4-}$,^{20,51,52} that support faster redox reactions and that can better compete with the fast electron–hole recombination in iron oxide.⁵³ Other options are the use of cocatalysts and templating scaffolds such as silica for the immobilization of nanoparticle photocatalysts.⁵⁴

3 Experimental Details

3.1 Chemicals

All reagents were obtained from Fisher Scientific. $\text{FeCl}_3 \cdot 6\text{H}_2\text{O}$ (99.9%), 12.1 N HCl (99.99%), NaOH (>97.0%) were used as obtained. Water was purified to at least 17.5 MΩ cm resistivity with a nano-pure filtration system. The NaIO_4 (99.0%, Fischer Scientific) was recrystallized from water. ITO powder (Alfa Aesar) 99.99% (metals basis) was used as obtained.

3.2 Synthesis

Iron (III) oxide hydroxide nanoparticles were synthesized following a literature reaction.³⁵ A 0.02M Fe^{3+} solution was created by adding 1.355 g $\text{FeCl}_3 \cdot 6\text{H}_2\text{O}$ to 250 mL of boiling 0.002M HCl in a round bottom flask attached to a condenser apparatus. This solution was boiled for an additional 30 min, at which time the flask was removed from heat and gradually cooled to room temperature. Samples for photocatalytic testing were taken directly from the suspension without further workup.

3.3 Characterization

XRD measurements were performed with a Rigaku MiniFlex600 with a standard sealed-tube Cu-K_α ($\lambda = 1.5418$ Å) source and a dTex ultra high-speed silicon strip detector with a nickel K_β filter. The sample was run on a Si_{510} single-crystal zero background plate and the energy window of the detector was set to reduce fluorescence from the iron in the sample. TEM images were collected on a Philips CM120 Biotwin Lens and Gatan MegaScan (model 794/20) digital camera (2 K \times 2 K). Samples were prepared by soaking carbon film coated copper grids in a suspension of the $\beta\text{-FeO(OH)}$ nanoparticles. The grids were then rinsed with high purity water and air-dried.

Particle size histograms were measured by dynamic light scattering using a Malvern Zetasizer Nano ZS90 equipped with a 633 nm laser. Samples for the zetasizer were prepared by a 1:10 dilution of the solution in nanopure (17.9 MΩ purified) water. Kubelka–Munk spectra were recorded using a Thermo Scientific Evolution 220 UV/Vis spectrometer. Sample films were dried onto white filter paper, and spectra were recorded using an integration sphere. SPV measurements were performed under 10^{-3} mbar vacuum and were obtained using a vibrating gold Kelvin probe (3 mm diameter, Delta PHI Besocke) mounted inside a home-built vacuum chamber and a Kelvin control 07 (Delta PHI Besocke) with a sensitivity of 1 mV. The sample-probe distance was kept consistent (ca. 1 mm). Particle films were prepared by dropping 0.5 mL of the sol onto an ITO covered FTO slide. The porous ITO coating was prepared by sonication of ITO powder in ethanol (5 mg/mL) followed by drop casting the slurry on a 1 cm² taped portion of the FTO slide and allowed to dry in air followed by annealing at 550°C for 3 h. Hematite nano-wire films were prepared as described in a previous publication.⁵⁰ Films were illuminated through the Kelvin probe with monochromatic light from a 300 W Xe lamp filtered through an Oriel Cornerstone 130 monochromator (light intensity range: 0.1 to 0.3 mW/cm²). The photovoltage spectra were corrected for drift effects by subtracting a dark scan. Photocatalytic oxygen evolution experiments were conducted by adjusting the pH of a solution of NaIO₄ with 2.0 M NaOH and then adding a determined amount of β-FeO(OH) nanoparticles (18 to 50 mg) from a sol with a gravimetrically determined concentration. This mixture was then placed in a quartz round-bottom flask and purged with Ar gas five times and applying reduced pressure (20 mbar) between purges. The solution was irradiated with light from a 300 W Xe arc lamp filtered through a 400 nm long pass filter (0.22M NaNO₂). Power densities were measured using an International Light IL1400BL photometer equipped with a GaAsP detector in the 280 to 660 nm sensitivity range. The irradiation system was connected to a Varian 3800 gas chromatograph (with a 60/80 Å molecular sieve column and a thermal conductivity detector). Quantum efficiency measurements were conducted under illumination from a 400 nm LED (460 mW cm⁻², 1.01×10^{18} photon cm⁻² s⁻¹).

Acknowledgments

This research was funded by NSF (Grant # 1152250 and 1133099) and by Research Corporation for Science Advancement (Scialog). We thank Ting Guo for access to the Zetasizer and Joshua Greenfield for X-ray diffraction measurements.

References

1. N. S. Lewis and D. G. Nocera, “Powering the planet: chemical challenges in solar energy utilization,” *Proc. Natl. Acad. Sci. U. S. A.* **103**, 15729–15735 (2006).
2. J. R. McKone, N. S. Lewis, and H. B. Gray, “Will solar-driven water-splitting devices see the light of day?” *Chem. Mater.* **26**, 407–414 (2014).
3. J. H. Kennedy and K. W. Frese, “Photooxidation of water at α-Fe₂O₃ electrodes,” *J. Electrochem. Soc.* **125**, 709–714 (1978).
4. K. L. Hardee and A. J. Bard, “Semiconductor electrodes: V. the application of chemically vapor deposited iron oxide films to photosensitized electrolysis,” *J. Electrochem. Soc.* **123**, 1024–1026 (1976).
5. K. Sivula, “Nanostructured α-Fe₂O₃ photoanodes,” Chapter 4 in *Photoelectrochemical Hydrogen Production*, R. van de Krol and M. Grätzel, Eds., Vol. **102**, pp. 121–156, Springer, United States (2012).
6. A. Annamalai et al., “Bifunctional TiO₂ underlayer for α-Fe₂O₃ nanorod based photoelectrochemical cells: enhanced interface and Ti⁴⁺ doping,” *J. Mater. Chem. A* **3**, 5007–5013 (2015).
7. I. Kondofersky et al., “Electron collection in host-guest nanostructured hematite photoanodes for water splitting: the influence of scaffold doping density,” *ACS Appl. Mater. Interfaces* **7**, 4623–4630 (2015).
8. P. Zhao et al., “The (0001) surfaces of α-Fe₂O₃ nanocrystals are preferentially activated for water oxidation by Ni doping,” *Phys. Chem. Chem. Phys.* **17**, 26797–26803 (2015).

9. P. S. Bassi et al., "Iron based photoanodes for solar fuel production," *Phys. Chem. Chem. Phys.* **16**, 11834–11842 (2014).
10. X. S. Zhang et al., "Improvement of hematite as photocatalyst by doping with tantalum," *J. Phys. Chem. C* **118**, 16842–16850 (2014).
11. G. Ruan et al., "Simultaneous doping and growth of Sn-doped hematite nanocrystalline films with improved photoelectrochemical performance," *RSC Adv.* **4**, 63408–63413 (2014).
12. J. Liu et al., "Ge-doped hematite nanosheets with tunable doping level, structure and improved photoelectrochemical performance," *Nano Energy* **2**, 328–336 (2013).
13. L. Wang et al., "Enhancing the water splitting efficiency of Sn-doped hematite nanoflakes by flame annealing," *Chem. Eur. J.* **20**, 77–82 (2014).
14. H. G. Cha et al., "Photocatalysis: progress using manganese-doped hematite nanocrystals," *New J. Chem.* **37**, 4004–4009 (2013).
15. C.-Y. Lee et al., "Si-doped Fe₂O₃ nanotubular/nanoporous layers for enhanced photoelectrochemical water splitting," *Electrochim. Commun.* **34**, 308–311 (2013).
16. B. Iandolo et al., "On the mechanism for nanoplasmonic enhancement of photon to electron conversion in nanoparticle sensitized hematite films," *Phys. Chem. Chem. Phys.* **15**, 4947–4954 (2013).
17. J. Y. Kim et al., "Single-crystalline, wormlike hematite photoanodes for efficient solar water splitting," *Sci. Rep.* **3**, 2681 (2013).
18. J. Liu et al., "General strategy for doping impurities (Ge, Si, Mn, Sn, Ti) in hematite nanocrystals," *J. Phys. Chem. C* **116**, 4986–4992 (2012).
19. A. Kahn, "Fermi level, work function and vacuum level," *Mater. Horiz.* **3**, 7–10 (2016).
20. B. Klahr et al., "Competitive photoelectrochemical methanol and water oxidation with hematite electrodes," *ACS Appl. Mater. Interfaces* **7**, 7653–7660 (2015).
21. G. M. Carroll, D. K. Zhong, and D. R. Gamelin, "Competitive photoelectrochemical methanol and water oxidation with hematite electrodes," *Energy Environon. Sci.* **8**, 577–584 (2015).
22. B. Iandolo et al., "Correlating flat band and onset potentials for solar water splitting on model hematite photoanodes," *RSC Adv.* **5**, 61021–61030 (2015).
23. O. Zandi and T. W. Hamann, "The potential versus current state of water splitting with hematite," *Phys. Chem. Chem. Phys.* **17**, 22485–22503 (2015).
24. X. Sala et al., "Molecular water oxidation mechanisms followed by transition metals: state of the art," *Acc. Chem. Res.* **47**, 504–516 (2014).
25. K. Sivula, "Metal oxide photoelectrodes for solar fuel production, surface traps, and catalysis," *J. Phys. Chem. Lett.* **4**, 1624–1633 (2013).
26. K. M. H. Young et al., "Photocatalytic water oxidation with hematite electrodes," *Catal. Sci. Technol.* **3**, 1660–1671 (2013).
27. B. Klahr et al., "Electrochemical and photoelectrochemical investigation of water oxidation with hematite electrodes," *Energy Environ. Sci.* **5**, 7626–7636 (2012).
28. A. Hellman and R. G. S. Pala, "First-principles study of photoinduced water-splitting on Fe₂O₃," *J. Phys. Chem. C* **115**, 12901–12907 (2011).
29. M. A. Gondal et al., "Production of hydrogen and oxygen by water splitting using laser induced photo-catalysis over Fe₂O₃," *Appl. Catal. A* **268**, 159–167 (2004).
30. J. Kiwi and M. Gratzel, "Light-induced hydrogen formation and photo-uptake of oxygen in colloidal suspensions of α -Fe₂O₃," *J. Chem. Soc. Faraday Trans. I* **83**, 1101–1108 (1987).
31. S. Chatterjee, S. Sarkar, and S. Bhattacharyya, "Size effect in the photochemical generation of hydrogen from water by colloidal Fe₂O₃ particles," *J. Photochem. Photobiol. A* **72**, 183–187 (1993).
32. T. Ohmori et al., "Photocatalytic oxygen evolution on α -Fe₂O₃ films using Fe³⁺ ion as a sacrificial oxidizing agent," *Phys. Chem. Chem. Phys.* **2**, 3519–3522 (2000).
33. T. K. Townsend et al., "Photocatalytic water oxidation with suspended α -Fe₂O₃ particles—effects of nanoscaling," *Energy Environ. Sci.* **4**, 4270–4275 (2011).
34. F. Le Formal et al., "Back electron—hole recombination in hematite photoanodes for water splitting," *J. Am. Chem. Soc.* **136**, 2564–2574 (2014).
35. T. P. Raming et al., "The synthesis and magnetic properties of nanosized hematite (α -Fe₂O₃) particles," *J. Colloid Interface Sci.* **249**, 346–350 (2002).

36. K. L. Chen, S. E. Mylon, and M. Elimelech, "Aggregation kinetics of alginate-coated hematite nanoparticles in monovalent and divalent electrolytes," *Environ. Sci. Technol.* **40**, 1516–1523 (2006).
37. Y. T. He, J. Wan, and T. Tokunaga, "Kinetic stability of hematite nanoparticles: the effect of particle sizes," *J. Nanopart. Res.* **10**, 321–332 (2008).
38. A. J. Bard and H. Lund, *Encyclopedia of Electrochemistry of the Elements*, M. Dekker, New York (1973).
39. A. Mills et al., "Periodate—an alternative oxidant for testing potential water oxidation catalysts," *J. Mater. Chem. A* **4**, 2863–2872 (2016).
40. S. U. M. Khan and J. Akikusa, "Photoelectrochemical splitting of water at nanocrystalline n-Fe₂O₃ thin-film electrodes," *J. Phys. Chem. B* **103**, 7184–7189 (1999).
41. H. Dau et al., "The mechanism of water oxidation: from electrolysis via homogeneous to biological catalysis," *ChemCatChem* **2**, 724–761 (2010).
42. A. Kay, I. Cesar, and M. Grätzel, "New benchmark for water photooxidation by nanostructured α -Fe₂O₃ films," *J. Am. Chem. Soc.* **128**, 15714–15721 (2006).
43. P. Peerakiatkhajohn et al., "Stable hematite nanosheet photoanodes for enhanced photoelectrochemical water splitting," *Adv. Mater.* (2016).
44. X. Guo, L. Wang, and Y. Tan, "Hematite nanorods Co-doped with Ru cations with different valence states as high performance photoanodes for water splitting," *Nano Energy* **16**, 320–328 (2015).
45. F. Osterloh, "Nanoscale effects in water splitting photocatalysis," *Top. Curr. Chem.* **371**, 105–142 (2016).
46. J. Wang, J. Zhao, and F. E. Osterloh, "Photochemical charge transfer observed in nanoscale hydrogen evolving photocatalysts using surface photovoltage spectroscopy," *Energy Environ. Sci.* **8**, 2970–2976 (2015).
47. J. Zhao and F. E. Osterloh, "Photochemical charge separation in nanocrystal photocatalyst films: insights from surface photovoltage spectroscopy," *J. Phys. Chem. Lett.* **5**, 782–786 (2014).
48. J. Wang and F. E. Osterloh, "Limiting factors for photochemical charge separation in BiVO₄/Co₃O₄, a highly active photocatalyst for water oxidation in sunlight," *J. Mater. Chem. A* **2**, 9405–9411 (2014).
49. E. Muthuswamy et al., "Thiol-capped germanium nanocrystals: preparation and evidence for quantum size effects," *Chem. Mater.* **26**, 2138–2146 (2014).
50. T. L. Shelton et al., "Photochemistry of hematite photoanodes under zero applied bias," *Appl. Catal. A: General* **521**, 168–173 (2016).
51. O. Zandi et al., "Enhanced charge separation and collection in high-performance electro-deposited hematite films," *Chem. Mater.* **28**, 765–771 (2016).
52. O. Zandi and T. W. Hamann, "Enhanced water splitting efficiency through selective surface state removal," *J. Phys. Chem. Lett.* **5**, 1522–1526 (2014).
53. H. Dotan et al., "Probing the photoelectrochemical properties of hematite (α -Fe₂O₃) electrodes using hydrogen peroxide as a hole scavenger," *Energy Environ. Sci.* **4**, 958–964 (2011).
54. H. Zhou et al., "Assembly of core-shell structures for photocatalytic hydrogen evolution from aqueous methanol," *Chem. Mater.* **22**, 3362–3368 (2010).

Frank E. Osterloh is an inorganic chemist working on particle-based solar energy conversion devices and nanostructured materials. He received his PhD in chemistry in 1997 after completing studies on iron sulfur clusters and nickel thiolate complexes under the guidance of the late Prof. Siegfried Pohl at the Carl von Ossietzky University in Oldenburg, Germany. His postdoctoral work with Prof. Richard H. Holm at Harvard University centered on molybdenum iron sulfur clusters.

Biographies for the other authors are not available.